nature communications

Article

https://doi.org/10.1038/s41467-024-53101-y

Learning quantum properties from short-range correlations using multi-task networks

Received: 7 November 2023

Accepted: 30 September 2024

Published online: 11 October 2024

Check for updates

Ya-Dong Wu [1,2,7], Yan Zhu [2,7] ✉, Yuexuan Wang [3,4] & Giulio Chiribella [2,5,6] ✉

Characterizing multipartite quantum systems is crucial for quantum computing and many-body physics. The problem, however, becomes challenging when the system size is large and the properties of interest involve correlations among a large number of particles. Here we introduce a neural network model that can predict various quantum properties of many-body quantum states with constant correlation length, using only measurement data from a small number of neighboring sites. The model is based on the technique of multi-task learning, which we show to offer several advantages over traditional single-task approaches. Through numerical experiments, we show that multi-task learning can be applied to sufficiently regular states to predict global properties, like string order parameters, from the observation of short-range correlations, and to distinguish between quantum phases that cannot be distinguished by single-task networks. Remarkably, our model appears to be able to transfer information learnt from lower dimensional quantum systems to higher dimensional ones, and to make accurate predictions for Hamiltonians that were not seen in the training.

The experimental characterization of many-body quantum states is an essential task in quantum information and computation. Neural networks provide a powerful approach to quantum state characterization[1–4], enabling a compact representation of sufficiently structured quantum states[5]. In recent years, different types of neural networks have been successfully utilized to predict properties of quantum systems, including quantum fidelity[6–8] and other measures of similarity[9,10], quantum entanglement[11–13], entanglement entropy[1,14,15], two-point correlations[1,2,14] and Pauli expectation values[4,16], as well as to identify phases of matter[17–21].

A challenge in characterizing multiparticle quantum systems is that the number of measurement settings rapidly increases with the system size. Randomized measurement techniques[22–30] provide an effective way to predict the properties of generic quantum states by using a reduced number of measurement settings, randomly sampled from the set of products of single particle observables. In the special case of many-body quantum systems subject to local interactions, however, sampling from an even smaller set of measurements may be possible, due to the additional structure of the states under consideration, which may enable a characterization of the state based only on short-range correlations, that is, correlations involving only a small number of neighboring sites. The use of short-range correlations has been investigated for the purpose of quantum state tomography[31–35] and entanglement detection[36,37]. A promising approach is to employ neural networks to predict global quantum properties directly from data obtained by sampling over a set of short-range correlations.

In this paper, we develop a neural network model for predicting various properties of quantum many-body states from short-range correlations. Our model utilizes the technique of multi-task learning[38] to generate concise state representations that integrate diverse types of information. In particular, the model can integrate information obtained from few-body measurements into a representation of the

[1]John Hopcroft Center for Computer Science, Shanghai Jiao Tong University, Shanghai, China. [2]QICI Quantum Information and Computation Initiative, Department of Computer Science, The University of Hong Kong, Pokfulam Road, Hong Kong, Hong Kong. [3]AI Technology Lab, Department of Computer Science, The University of Hong Kong, Pokfulam Road, Hong Kong, Hong Kong. [4]College of Computer Science and Technology, Zhejiang University, Hangzhou, Zhejiang Province, China. [5]Department of Computer Science, Parks Road, Oxford, United Kingdom. [6]Perimeter Institute for Theoretical Physics, Waterloo, Ontario, Canada. [7]These authors contributed equally: Ya-Dong Wu, Yan Zhu. ✉e-mail: yzhu2@cs.hku.hk; giulio@cs.hku.hk

overall quantum state, in a way that is reminiscent of the quantum marginal problem[39–41]. The state representations produced by our model are then used to learn new physical properties that were not seen during the training, including global properties such as string order parameters and many-body topological invariants[42].

For ground states with short-range correlations, we find that our model accurately predicts nonlocal features using only measurements on a few nearby particles. With respect to traditional, single-task neural networks, our model achieves more precise predictions with comparable amounts of input data and enables a direct, unsupervised classification of symmetry-protected topological (SPT) phases that could not be distinguished in the single-task approach. In addition, we find that, after the training is completed, the model can be applied to quantum states and Hamiltonians outside the original training set, and even to quantum systems of higher dimension. This strong performance on out-of-distribution states suggests that the multi-task approach is a promising tool for exploring the next frontier of intermediate-scale quantum systems.

Results

Multi-task framework for quantum properties

Consider the scenario where an experimenter has access to multiple copies of an unknown quantum state ρ_θ, characterized by some physical parameters θ. For example, ρ_θ could be a ground state of many-body local Hamiltonian depending on θ. The experimenter's goal is to predict a set of properties of the quantum state, such as the expectation values of some observables, or some nonlinear functions, such as the von Neumann entropy. The experimenter is able to perform a restricted set of quantum measurements, denoted by $\mathcal{M}$. Each measurement $\mathbf{M} \in \mathcal{M}$ is described by a positive operator-valued measure (POVM) $\mathbf{M} = (M_j)$, where the index j labels the measurement outcome, each M_j is a positive operator acting on the system's Hilbert space, and the normalization condition $\sum_j M_j = I$ is satisfied. In general, the measurement set $\mathcal{M}$ may not be informationally complete. For multipartite systems, we will typically take $\mathcal{M}$ to consist of short-range measurements, that is, local measurements performed on a small number of neighboring systems, although this choice is not a necessary part of our multi-task learning framework. It is also worth noting that choosing short-range measurements for the set $\mathcal{M}$ does not necessarily mean that the experimenter has to physically isolate a subset of neighboring systems before doing their measurements. The access to short-range measurement statistics can obtained, *e.g.* from product measurements performed jointly on all systems, by discarding the outcomes generated from systems outside the subset of interest. In this way, a single product measurement performed jointly on all systems can provide data to multiple short-range measurements.

To collect data, the experimenter randomly picks a subset of measurements $\mathcal{S} \subset \mathcal{M}$, and performs them on different copies of the state ρ_θ. We will denote by s the number of measurements in $\mathcal{S}$, and by $\mathbf{M}_i := \left(M_{ij}\right)$ the i-th POVM in $\mathcal{S}$. For simplicity, if not specified otherwise, we assume that each measurement in $\mathcal{S}$ is repeated sufficiently many times, so that the experimenter can reliably estimate the outcome distribution $\mathbf{d}_i := (d_{ij})$, where $d_{ij} := \mathrm{tr}(\rho M_{ij})$.

The experimenter's goal is to predict multiple quantum properties of ρ_θ using the outcome distributions $(\mathbf{d}_i)_{i=1}^s$. This task is achieved by a neural network that consists of an encoder and multiple decoders, where the encoder $\mathcal{E}$ produces a representation of quantum states and the k-th decoder $\mathcal{D}_k$ produces a prediction of the k-th property of interest. Due to their roles, the encoder and decoders are also known as representation and prediction networks, respectively.

The input of the representation network $\mathcal{E}$ is the outcome distribution $\mathbf{d}_i$, together with a parametrization of the corresponding measurement $\mathbf{M}_i$, hereafter denoted by $\mathbf{m}_i$. From the pair of data $(\mathbf{d}_i, \mathbf{m}_i)$, the network produces a state representation $\mathbf{r}_i := \mathcal{E}(\mathbf{d}_i, \mathbf{m}_i)$. To combine the state representations arising from different measurements in $\mathcal{S}$, the network computes the average $\mathbf{r} := \frac{1}{s}\sum_{i=1}^s \mathbf{r}_i$. At this point, the vector $\mathbf{r}$ can be viewed as a representation of the unknown quantum state ρ.

Each prediction network $\mathcal{D}_k$ is dedicated to a different property of the quantum state. In the case of multipartite quantum systems, we include the option of evaluating the property on a subsystem, specified by a parameter q. We denote by $f_{k,q}(\rho_\theta)$ the correct value of the k-th property of subsystem q when the total system is in the state ρ_θ. Upon receiving the state representation $\mathbf{r}$ and the subsystem specification q, the prediction network produces an estimate $\mathcal{D}_k(\mathbf{r}, q)$ of the value $f_{k,q}(\rho)$.

The representation network and all the prediction networks are trained jointly, with the goal of minimizing the total prediction error on a set of fiducial states. The fiducial states are chosen by randomly sampling a set of physical parameters $(\theta_l)_{l=1}^L$. For each fiducial state ρ_{θ_l}, we independently sample a set of measurements $\mathcal{S}_l$ and calculate the outcome distributions for each measurement in the set $\mathcal{S}_l$. We randomly choose a subset of properties $\mathcal{K}_l$ for each ρ_{θ_l}, where each property $k \in \mathcal{K}_l$ corresponds to a set of subsystems $\mathcal{Q}_k$, and then calculate the correct values of the quantum properties $\{f_{k,q}(\rho_{\theta_l})\}$ for all properties $k \in \mathcal{K}_l$ associated with subsystems $q \in \mathcal{Q}_k$. The training data may be either classically simulated or gathered by actual measurements on the set of fiducial states, or it could also be obtained by any combination of these two approaches.

During the training, we do not provide the model with any information about the physical parameters θ_l or about the functions $f_{k,q}$. Instead, the internal parameters of the neural networks are jointly optimized in order to minimize the prediction errors $|\mathcal{D}_k\left(1/s\sum_{i=1}^s \mathcal{E}(\{\mathbf{d}_i, \mathbf{m}_i\}), q\right) - f_{k,q}(\rho_\theta)|$ summed over all the fiducial states, all chosen properties, and all chosen subsystems.

After the training is concluded, our model can be used for predicting quantum properties, either within the set of properties seen during training or outside this set. The requested properties are predicted on a new, unknown state ρ_θ, and even out-of-distribution state ρ that has a structural similarity with the states in the original distribution, e.g., a ground state of the same type of Hamiltonian, but for a quantum system with a larger number of particles.

The high-level structure of our model is illustrated in Fig. 1, while the details of the neural networks are presented in Methods.

Learning ground states of Cluster-Ising model

We first test the performance of our model on a relatively small system of $N = 9$ qubits whose properties can be explicitly calculated. For the state family, we take the ground states of one-dimensional cluster-Ising model[43]

$$H_{\mathrm{cI}} = -\sum_{i=1}^{N-2} \sigma_i^z \sigma_{i+1}^x \sigma_{i+2}^z - h_1 \sum_{i=1}^{N} \sigma_i^x - h_2 \sum_{i=1}^{N-1} \sigma_i^x \sigma_{i+1}^x. \tag{1}$$

The ground state falls in one of three phases, depending on the values of the parameters (h_1, h_2). The three phases are: the SPT phase, the paramagnetic phase, and the antiferromagnetic phase. SPT phase can be distinguished from two other phases by measuring the string order parameter[44,45] $\langle \tilde{S} \rangle := \langle \sigma_1^z \sigma_2^x \sigma_4^x \ldots \sigma_{N-3}^x \sigma_{N-1}^x \sigma_N^z \rangle$, which is a global property involving $(N+3)/2$ qubits.

We test our network model on the ground states corresponding to a 64×64 square grid in the parameter region $(h_1, h_2) \in [0, 1.6] \times [-1.6, 1.6]$. For the set of accessible measurements $\mathcal{M}$, we take all possible three-nearest-neighbor Pauli measurements, corresponding to the observables $\sigma_i^\alpha \sigma_{i+1}^\beta \sigma_{i+2}^\gamma$, where $i \in \{1, 2, \ldots, N-2\}$ and $\alpha, \beta, \gamma \in \{x, y, z\}$. It is worth noting that, when two measurements

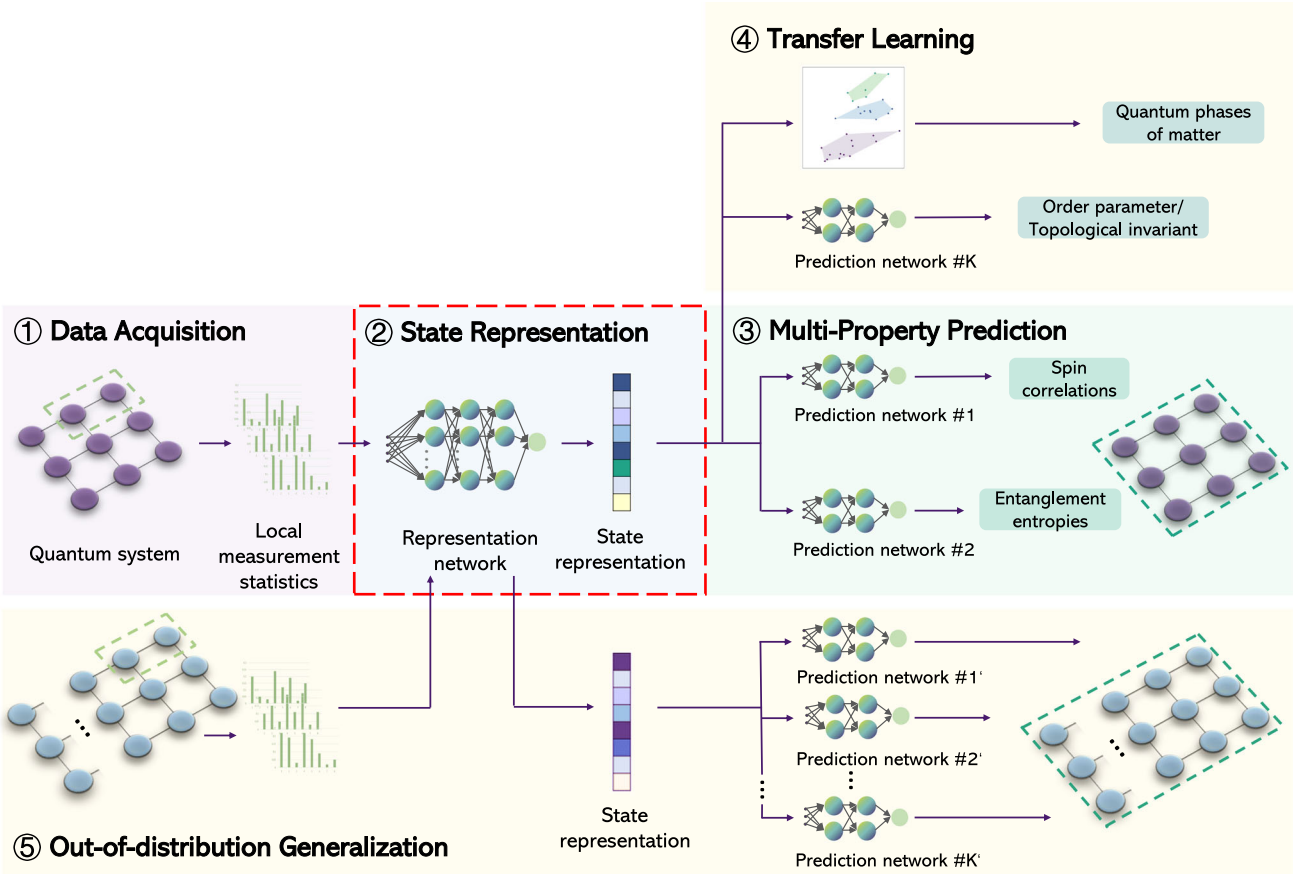

Fig. 1 | Flowchart of our multi-task neural network. In the data acquisition phase (**1**), the experimenter performs short-range local measurements on the system of interest. The resulting data is used to produce a concise representation of the quantum state (**2**). The state representation is then fed into a set of prediction networks, each of which generates predictions for a given type of quantum property (**3**). After the state representation network and prediction networks are jointly trained, the state representations are employed in new tasks, such as unsupervised classification of quantum phases of matter, or prediction of order parameters and topological invariants (**4**). Once trained, the overall model can generally be applied to out-of-distribution quantum states and higher-dimensional quantum systems (**5**).

$\mathbf{M} \neq \mathbf{M}'$ act on disjoint qubit triplets or coincide at overlapping qubits, these measurements can be performed simultaneously on a single copy of the state, thereby reducing the number of data collection rounds.

In general, increasing the range of the correlations among Pauli measurements can increase the performance of the network. For example, using the correlations from Pauli measurements on triplets of neighboring qubits (as described above) leads to a better performance than using correlations from Pauli measurements on pairs of neighboring qubits, as illustrated in Supplementary Note 5. On the other hand, increasing the range of the correlations also increases the size of the input to the neural network, making the training more computationally expensive.

For the prediction tasks, we consider two properties: (A1) the two-point correlation function $C_{1j}^{\alpha} := \langle \sigma_1^{\alpha} \sigma_j^{\alpha} \rangle_{\rho}$, where $1 < j \leq N$ and $\alpha = x, z$; (A2) the Rényi entanglement entropy of order two $S_A := -\log_2(\mathrm{tr}\rho_A^2)$ for subsystem $A = [1, 2, \ldots, i]$, where $1 \leq i < N$. Both properties (A1) and (A2) can be either numerically evaluated, or experimentally estimated by preparing the appropriate quantum state and performing randomized measurements[27].

We train our neural network with respect to the fiducial ground states corresponding to 300 randomly chosen points from our 4096-element grid. For each fiducial state, we provide the neural network with the outcome distributions of $s = 50$ measurements, randomly chosen from the 243 measurements in $\mathcal{M}$. Half of these fiducial states randomly chosen from the whole set are labeled by the values of property (A1) and the other half are labeled by property (A2). After training is concluded, we apply our trained model to predicting properties (A1)-(A2) for all remaining ground states corresponding to points on the grid. For each test state, the representation network is provided with the outcome distributions on $s = 50$ measurement settings randomly chosen from $\mathcal{M}$.

Figure 2a illustrates the coefficient of determination (R^2), averaged over all test states, for each type of property. Notably, all the values of R^2 observed in our experiments are above 0.95. Our network makes accurate predictions even near the boundary between the SPT phase and paramagnetic phase, in spite of the fact that phase transitions typically make it more difficult to capture the ground state properties from limited measurement data. For a ground state close to the boundary, marked by a star in the phase diagram (Fig. 3d), the predictions of the entanglement entropy $\mathcal{S}_A$ and spin correlation C_{1j}^{z} are close to the corresponding ground truths, as shown in Fig. 2d and e, respectively.

In general, the accuracy of the predictions depends on the number of samplings for each measurement as well as the number of measurement settings. For our experiments, the dependence is illustrated in Fig. 2b and c.

To examine whether our multi-task neural network model enhances the prediction accuracy compared to single-task networks, we perform ablation experiments[46]. We train three individual single-task neural networks as our baseline models, each of which predicts spin correlations in Pauli-x axis, spin correlations in Pauli-z axis, and

https://doi.org/10.1038/s41467-024-53101-y

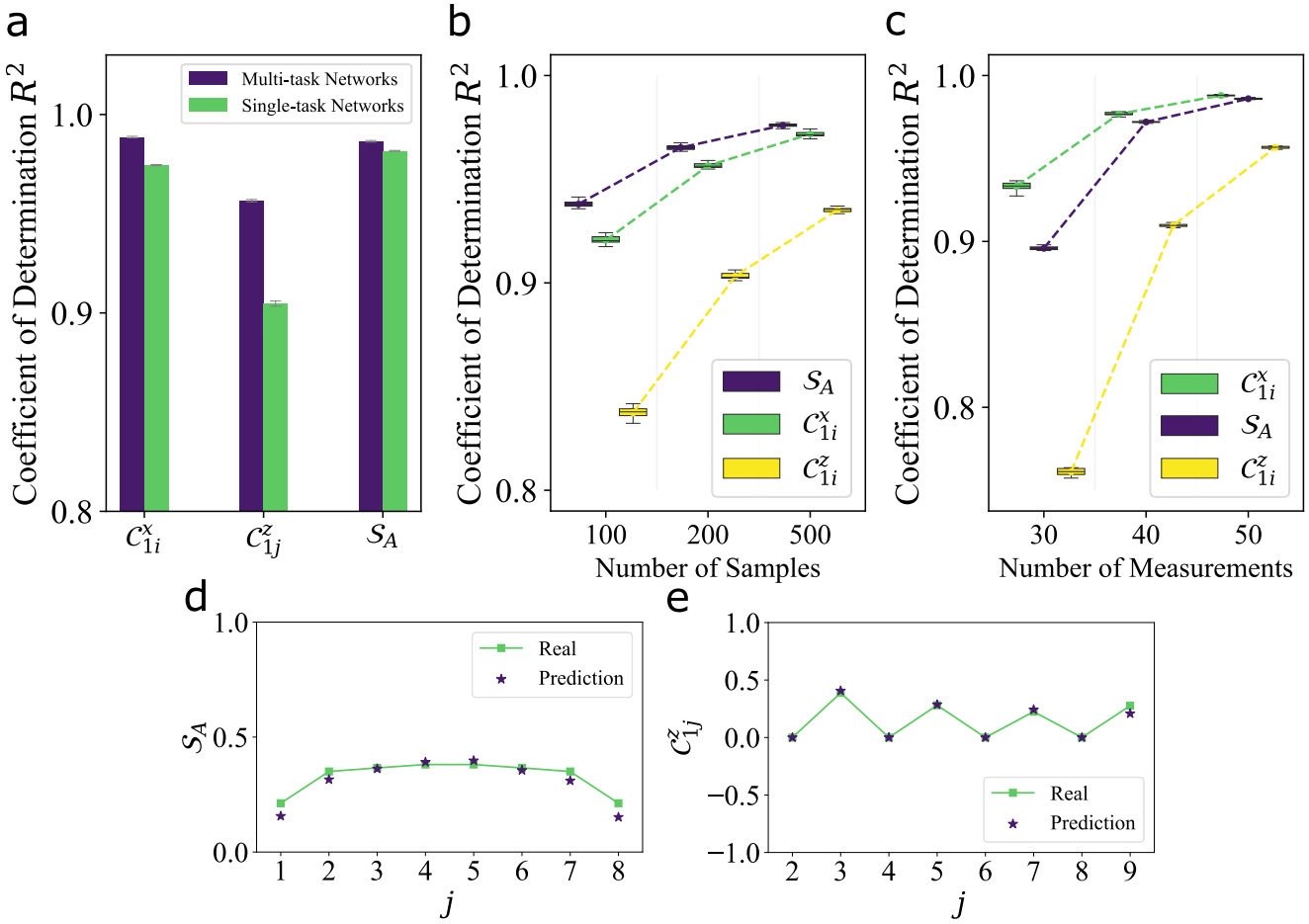

Fig. 2 | Predicting properties of ground states of cluster-Ising model. Subfigure (**a**) compares the prediction accuracy between our multi-task model and single-task models for predicting two-point correlation functions $\mathcal{C}_{ij}^{x}$ and $\mathcal{C}_{ij}^{z}$, and entanglement entropy $\mathcal{S}_A$. The error bars show the standard deviations of R^2 for different test states. Subfigures (**b** and **c**) show how the number of samples for each measurement and the number of measurements affect the coefficient of determination for the predictions of $\mathcal{S}_A$, $\mathcal{C}_{1j}^{x}$ and $\mathcal{C}_{1j}^{z}$, respectively, via boxplots[59]. Subfigures (**d** and **e**) show the predictions of $\mathcal{S}_A$ and $\mathcal{C}_{1j}^{z}$ for a ground state near phase transition marked by a red star in Subfigure 3**d**.

entanglement entropies, respectively. For each single-task neural network, the training provides the network with the corresponding properties for the 300 fiducial ground states, without providing any information about the other properties. After the training is concluded, we apply each single-task neural network to predict the corresponding properties on all the test states and use their predictions as baselines to benchmark the performance of our multi-task neural network. Figure 2a compares the values of R^2 for the predictions of our multi-task neural model with those of the single-task counterparts. The results demonstrate that learning multiple physical properties simultaneously enhances the prediction of each individual property.

Transfer learning to new tasks

We now show that the state representations produced by the encoder can be used to perform new tasks that were not encountered during the training phase. In particular, we show that state representations can be used to distinguish between the phases of matter associated to different values of the Hamiltonian parameters in an unsupervised manner. To this purpose, we project the representations of all the test states onto a two-dimensional (2D) plane using the t-distributed stochastic neighbor embedding (t-SNE) algorithm.

The results are shown in Fig. 3a. Every data point shows the exact value of the string order parameter, which distinguishes between the SPT phase and the other two phases. Quite strikingly, we find that the disposition of the points in the 2D representation matches the values of the string order parameter, even though no information about the string order parameters was provided during the training, and even though the string order is a global property, while the measurement data provided to the network came from a small number of neighboring sites.

A natural question is whether the accurate classification of phases of matter observed above is a consequence of the multi-task nature of our model. To shed light into this question, we compare the results of our multi-task network with those of single-task neural networks, feeding the state representations generated by these networks into the t-SNE algorithm to produce a 2D representation. The pattern of the projected state representations in Fig. 3b indicates that when trained only with the values of entanglement entropies, the neural network cannot distinguish between the paramagnetic phase and the antiferromagnetic phase. Interestingly, a single-task network trained only on the spin correlations can still distinguish the SPT phase from the other two phases, as shown in Fig. 3c. However, in the next section we see that applying random local gates induces errors in the single-task network, while the multi-task network still achieves a correct classification of the different phases.

Quantitatively, the values of the string order parameter can be extracted from the state representations using another neural

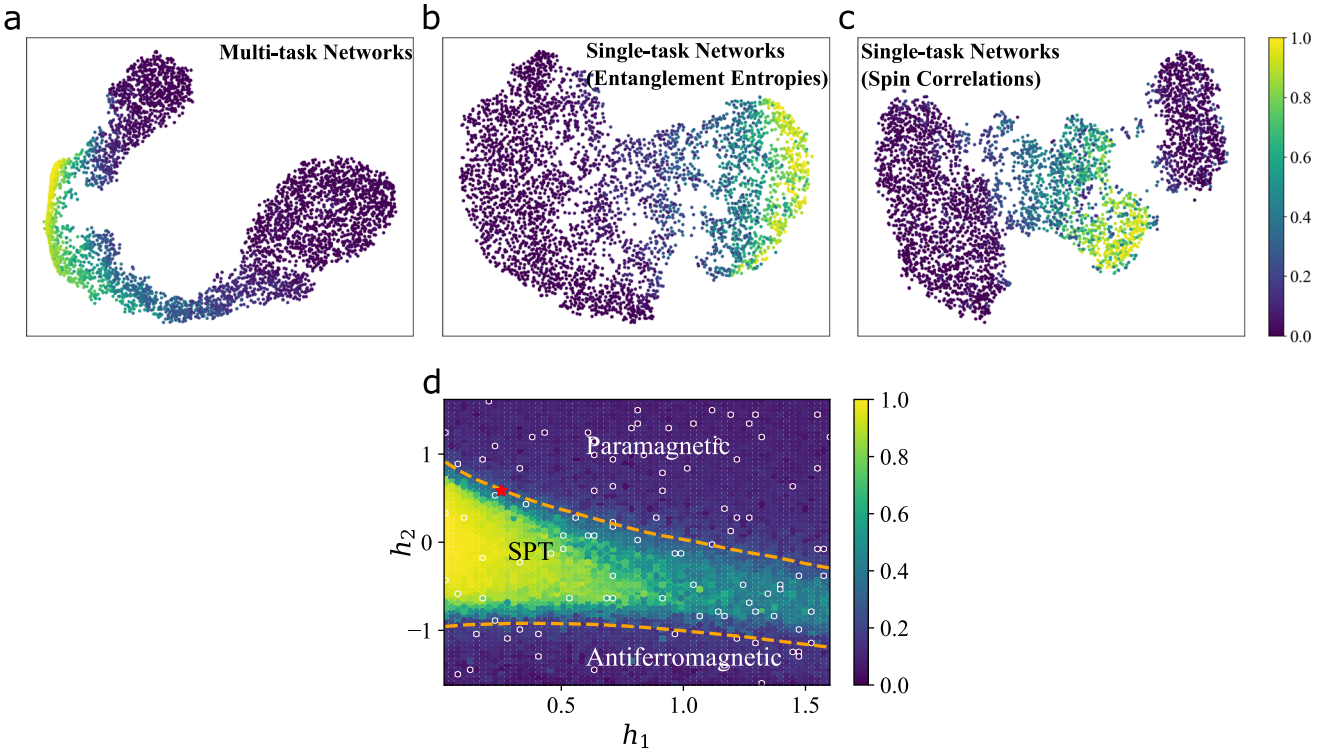

Fig. 3 | Transfer learning to predict properties of the ground states of the cluster-Ising model. Subfigures **a**, **b** and **c** illustrate the 2D projection of the state representations obtained with the t-SNE algorithm, where the color of each data point indicates the true value of the string order parameter $\langle \tilde{S} \rangle$ of the corresponding ground state. Subfigure (**a**) corresponds to the state representations produced for jointly predicting spin correlations and entanglement entropy. Subfigures (**b** and **c**) correspond to the state representations produced for separately predicting entanglement entropy and spin correlations, respectively. Subfigure (**d**) shows the predictions of $\langle \tilde{S} \rangle$ for the ground states corresponding to a 64 × 64 grid in parameter space, together with the true values of $\langle \tilde{S} \rangle$ for 100 randomly chosen states indicated by white circles, where the dashed curves are the phase boundaries between symmetry protected topological (SPT) phase and the other two phases.

network $\mathcal{N}$. To train this network, we randomly pick 100 reference states $\{\sigma_i\}$ out of the 300 fiducial states and minimize the error $\sum_{i=1}^{100} |\mathcal{N}(\mathbf{r}_{\sigma_i}) - \langle \tilde{S} \rangle_{\sigma_i}|$. Then, we use the trained neural network $\mathcal{N}$ to produce the prediction $\mathcal{N}(\mathbf{r}_\rho)$ of $\langle \tilde{S} \rangle_\rho$ for every other state ρ. The prediction for each ground state is shown in the phase diagram (Fig. 3d), where the 100 reference states are marked by white circles. The predictions are close to the true values of string order parameters, with the coefficient of determination between the predictions and the ground truth being 0.97. It is important to stress that, while the network $\mathcal{N}$ was trained on values of the string order parameter, the representation network $\mathcal{E}$ was not provided any information about this parameter. Note also that the values of the Hamiltonian parameters (h_1, h_2) are just provided in the figure for the purpose of visualization: in fact, no information about the Hamiltonian parameters was provided to the network during training or test. In Supplementary Note 5, we show that our neural network model trained for predicting entanglement entropy and spin correlations can also be transferred to other ground-state properties of the cluster-Ising model.

Generalization to out-of-distribution states

In the previous sections, we assumed that both the training and the testing states were randomly sampled from a set of ground states of the cluster-Ising model (1). In this subsection, we explore how a model trained on a given set of quantum states can generalize to states outside the original set in an unsupervised or weakly supervised manner.

Our first finding is that our model, trained on the ground states of the cluster-Ising model, can effectively cluster general quantum states in the SPT phase and the trivial phase (respecting the symmetry of bit flips at even/odd sites), without further training. Random quantum states in SPT (trivial) phase can be prepared by applying short-range symmetry-respecting local random quantum gates on a cluster state in the SPT phase (a product state $|+\rangle^{\otimes N}$ in the paramagnetic phase). For these random quantum states, we follow the same measurement strategy adopted before, feed the measurement data into our trained representation network, and use t-SNE to project the state representations onto a 2D plane.

When the quantum circuit consists of a layer of translation-invariant next-nearest neighbor symmetry-respecting random gates, our model successfully classifies the output states into their respective SPT phase and trivial phase in both cases, as shown by Fig. 4a. In contrast, feeding the same measurement data into the representation network trained only on spin correlations fails to produce two distinct clusters via t-SNE, as shown by Fig. 4b. While this neural network successfully classifies different phases for the cluster-Ising model, random local quantum gates confuse it. This failure is consistent with the recent observation that extracting linear functions of a quantum state is insufficient for classifying arbitrary states within SPT phase and trivial phase[26].

We then prepare more complex states by applying two layers of translation-invariant random gates consisting of both nearest neighbor and next-nearest neighbor gates preserving the symmetry onto the initial states. The results in Fig. 4c show that the state representations of these two phases remain different, but the boundary between them in the representation space is less clearly identified. Whereas, the neural network trained only on spin correlations fails to classify these two phases, as shown by Fig. 4d.

Finally, we demonstrate that our neural model, trained on the cluster-Ising model, can adapt to learn the ground states of a new,

https://doi.org/10.1038/s41467-024-53101-y

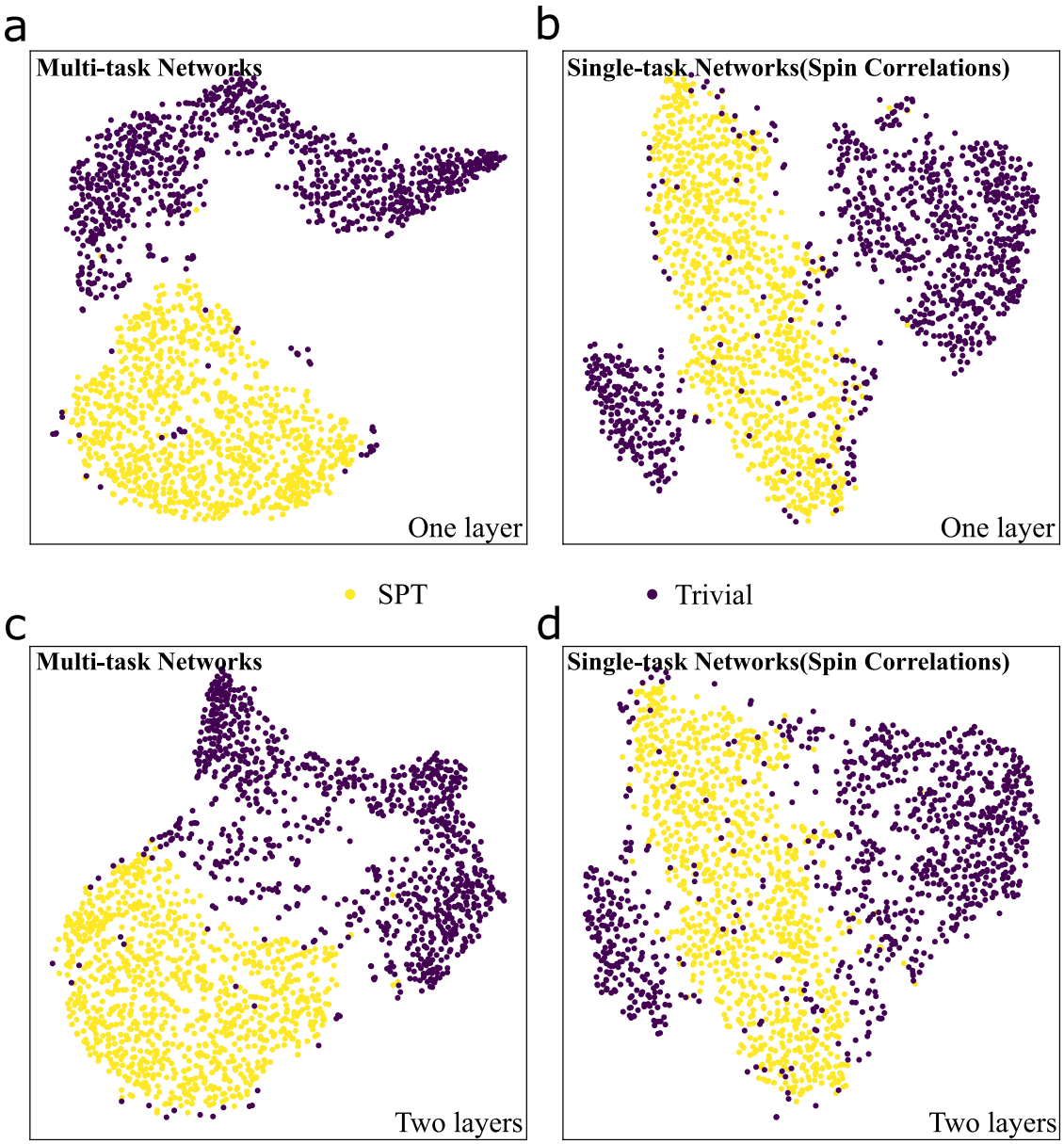

Fig. 4 | 2D projections of state representations for those states prepared by shallow random symmetric quantum circuits. Subfigures (**a** and **b**) correspond quantum states in the symmetry protected topological (SPT) and the trivial phases prepared by one layer of random quantum gates, and Subfigures (**c** and **d**) correspond quantum states in the SPT and the trivial phases prepared by two layers of random quantum gates. Subfigures (**a** and **c**) illustrate state representations produced by our multi-task neural network. Subfigures (**b** and **d**) illustrate state representations produced by the neural network trained only on spin correlations.

perturbed Hamiltonian[47]

$$H_{\mathrm{pcl}} = H_{\mathrm{cl}} + h_3 \sum_{i=1}^{N-1} \sigma_i^z \sigma_{i+1}^z. \tag{2}$$

This perturbation breaks the original symmetry, shifts the boundary of the cluster phase, and introduces a new phase of matter. In spite of these substantial changes, Fig. 5a shows that our model, trained on the unperturbed cluster-Ising model, successfully identifies the different phases, including the new phase from the perturbation. Moreover, using just 10 randomly chosen additional reference states (marked by white circles in Fig. 5b), the original prediction network can be adjusted to predict the values of $\langle \tilde{\mathcal{S}} \rangle$ from state representations. As shown in Fig. 5b, the predicted values closely match the ground truths in Fig. 5c, achieving a coefficient of determination of up to 0.956 between the predictions and the ground truths.

Learning ground states of XXZ model

We now apply our model to a larger quantum system, consisting of 50 qubits in ground states of the bond-alternating XXZ model[24]

$$\begin{aligned} H = J \sum_{i=1}^{N/2} \left(\sigma_{2i-1}^x \sigma_{2i}^x + \sigma_{2i-1}^y \sigma_{2i}^y + \delta \sigma_{2i-1}^z \sigma_{2i}^z\right) \\ + J' \sum_{i=1}^{N/2-1} \left(\sigma_{2i}^x \sigma_{2i+1}^x + \sigma_{2i}^y \sigma_{2i+1}^y + \delta \sigma_{2i}^z \sigma_{2i+1}^z\right), \end{aligned} \tag{3}$$

where J and J' are the alternating values of the nearest-neighbor spin couplings. We consider a set of ground states corresponding to a 21×21 square grid in the parameter region $(J/J', \delta) \in (0,3) \times (0,4)$. Depending on the ratio of J/J' and the strength of δ, the corresponding ground state falls into one of three possible phases: trivial SPT phase, topological SPT phase, and symmetry broken phase.

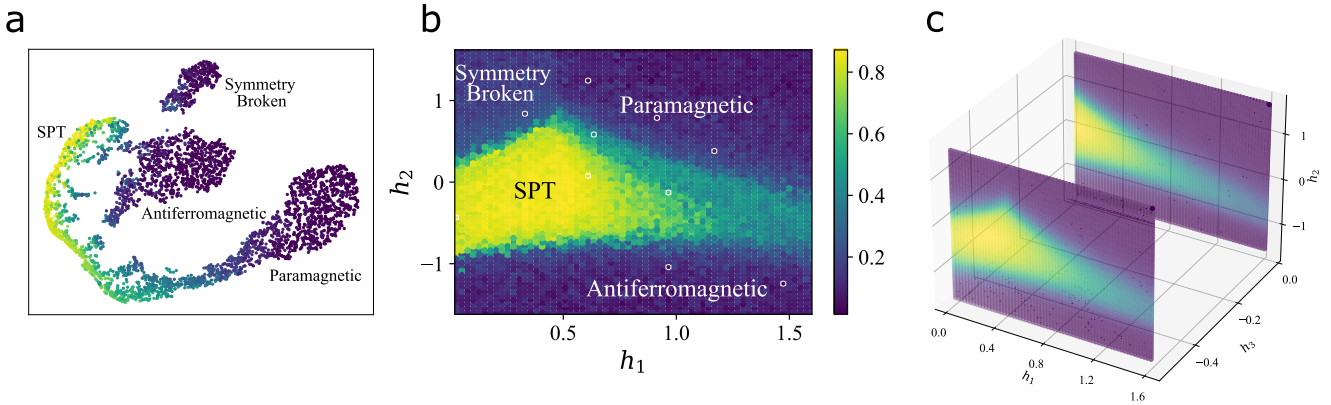

Fig. 5 | Prediction of properties of ground states of a perturbed Hamiltonian. Subfigure (**a**) illustrates the 2D projections of state representations for the ground states of the perturbed Hamiltonian, together with their true values of $\langle \bar{S} \rangle$. Subfigure (**b**) illustrates the predictions of $\langle \bar{S} \rangle$ using our adjusted neural network for the perturbed model. Subfigure (**c**) show the true values of string order parameters $\langle \bar{S} \rangle$ for both the original model (1) and the perturbed model (2).

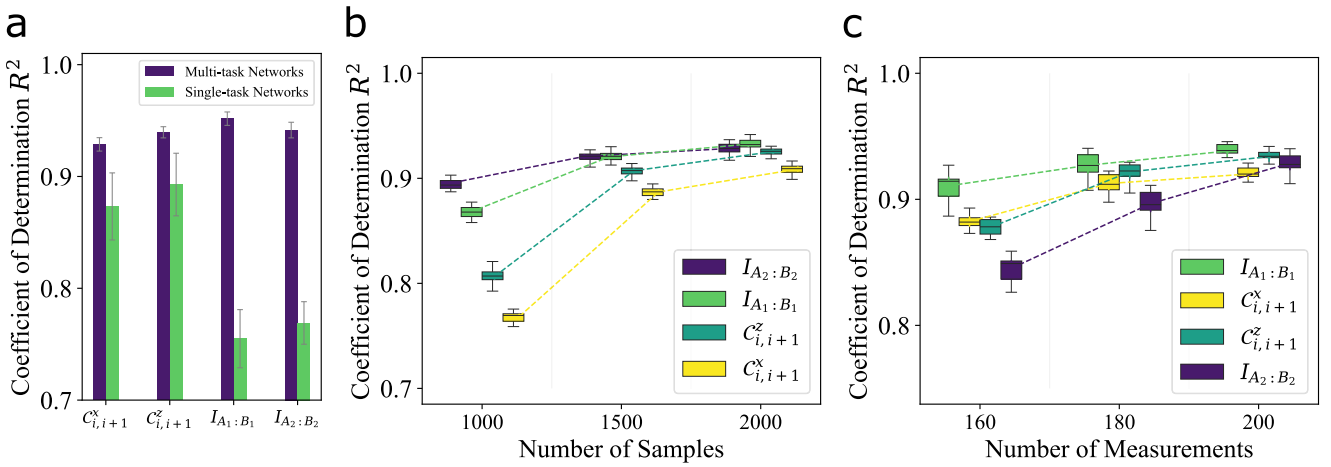

Fig. 6 | Predicting properties of 50 qubit ground states of bond-alternating XXZ model. Subfigure (**a**) compares the prediction accuracy between our multi-task model and single-task models for predicting spin correlations C^x_{ii+1} and C^z_{ii+1}, as well as Rényi mutual information $I_{A_1:B_1}$ and $I_{A_2:B_2}$, where A_1 = [22: 25], B_1 = [26: 29], A_2 = [21: 24] and B_2 = [25: 28] are all four-qubit subsystems. The error bars show the standard deviations of R^2 for different test states. Subfigure (**b** and **c**) show how the number of samples for each measurement and the number of measurements affect the coefficient of determination for the predictions of all the properties via boxplots.

Unlike the SPT phases of cluster-Ising model, the SPT phases of bond-alternating XXZ model cannot be detected by any string order parameter. Both SPT phases are protected by bond-center inversion symmetry, and detecting them requires a many-body topological invariant, called the partial reflection topological invariant[24] and denoted by

$$\mathcal{Z}_R := \frac{\mathrm{tr}(\rho_I \mathcal{R}_I)}{\sqrt{\left[\mathrm{tr}\left(\rho_{I_1}^2\right) + \mathrm{tr}\left(\rho_{I_2}^2\right)\right]/2}}. \tag{4}$$

Here, $\mathcal{R}_I$ is the swap operation on subsystem $I := I_1 \cup I_2$ with respect to the center of the spin chain, and $I_1 = [N/2 - 5, N/2 - 4, \ldots, N/2]$ and $I_2 = [N/2 + 1, N/2 + 2, \ldots, N/2 + 6]$ are two subsystems with six qubits.

For the set of possible measurements $\mathcal{M}$, we take all possible three-nearest-neighbor Pauli projective measurements, as we did earlier in the cluster-Ising model. For the prediction tasks, we consider two types of quantum properties: (B1) nearest-neighbor spin correlations $C^\beta_{i,i+1} := \langle \sigma^\beta_i \sigma^\beta_{i+1} \rangle (1 \le i \le N-1)$, where $\beta = x, z$; (B2) order-two Rényi mutual information $I_{A:B}$, where A and B are both 4-qubit subsystems: either A_1 = [22: 25], B_1 = [26: 29] or A_2 = [21: 24], B_2 = [25: 28].

We train our neural network with respect to the fiducial ground states corresponding to 80 pairs of $(J/J', \delta)$, randomly sampled from the 441-element grid. For each fiducial state, we provide the neural network with the probability distributions corresponding to s = 200 measurements randomly chosen from the 1350 measurements in $\mathcal{M}$. Half of the fiducial states randomly chosen from the entire set are labeled by the property of (B1), while the other half are labeled by the property of (B2). After the training is concluded, we use our trained model to predict both properties (B1) and (B2) for all the ground states in the grid.

Figure 6a demonstrates the strong predictive performance of our model, where the values of R^2 are above 0.92 for all properties averaged over test states. We benchmark the performances of our multi-task neural network with the predictions of single-task counterparts. Here each single-task neural network, the size of which is same as the multi-task network, aims at predicting one single physical property and is trained using the same set of measurement data of 80 fiducial states together with one of their properties: $C^x_{i,i+1}$, $C^z_{i,i+1}$, $I_{A_1:B_1}$ and $I_{A_2:B_2}$. Figure 6a compares the coefficients of determination for the predictions of both our multi-task neural network and the single-task neural networks, where each experiment is repeated multiple times over different sets of s = 200 measurements randomly chosen from $\mathcal{M}$. The

results indicate that our multi-task neural model not only achieves higher accuracy in the predictions of all properties, but also is much more robust to different choices of quantum measurements. As in the case of the cluster-Ising model, we also study how the number of quantum measurements s and the number of samplings for each quantum measurement affect the prediction accuracy of our neural network model, as shown by Fig. 6b and c. Additionally, in Supplementary Note 6 we test how the size of the quantum system affects the prediction accuracy given the same amount of local measurement data, and how the number of layers in the representation network affects the prediction accuracy. Interestingly, we observe that reducing the number of layers from four to two results in a significant decline in performance when predicting properties (B1) and (B2). This observation indicates that the depth of the network plays an important role in achieving effective multi-task learning of the bond-alternating XXZ ground states.

We show that, even in the larger-scale example considered in this section, the state representations obtained through multi-task training contain information about the quantum phases of matter. In Fig. 7a, we show the 2D-projection of the state representations. The data points corresponding to ground states in the topological SPT phase, the trivial SPT phase and the symmetry broken phase appear to be clearly separated into three clusters, while the latter two connected by a few data points corresponding to ground states across the phase boundary. A few points, corresponding to ground states near phase boundaries of the topological SPT phase, are incorrectly clustered by the t-SNE algorithm. The origin of the problem is that the correlation length of ground states near phase boundary becomes longer, and therefore the measurement statistics on nearest-neighbor-three qubit subsystems cannot capture sufficient information for predicting the correct phase of matter.

We further examine if the single-task neural networks above can correctly classify the three different phases of matter. We project the state representations produced by each single-task neural network onto 2D planes by the t-SNE algorithm, as shown by Fig. 7b and c. The pattern of projected representations in Fig. 7b implies that when trained only with the values of spin correlations, the neural network cannot distinguish the topological SPT phase from the trivial SPT phase. The pattern in Fig. 7c indicates that when trained solely with mutual information, the performance of clustering is slightly improved, but still cannot explicitly classify these two SPT phases. We also project the state representations produced by the neural network for predicting measurement outcome statistics[3] onto a 2D plane. The resulting pattern, shown in Fig. 7d, shows that the topological SPT phase and the trivial SPT phase cannot be correctly classified either. These observations indicate that a multi-task approach, including both the properties of mutual information and spin correlations, is necessary to capture the difference between the topological SPT phase and the trivial SPT phase.

The emergence of clusters related to different phases of matter suggests that the state representation produced by our network also contains quantitative information about the topological invariant $\mathcal{Z}_R$. To extract this information, we use an additional neural network, which maps the state representation into a prediction of $\mathcal{Z}_R$. We train this additional network by randomly selecting 60 reference states (marked by gray squares in Fig. 7e) out of the set of 441 fiducial states, and by minimizing the prediction error on the reference states. The predictions together with 60 exact values of the reference states are shown in Fig. 7e The absolute values of the differences between the predictions and ground truths are shown in Fig. 7f. The predictions are close to the ground truths, except for the ground states near the phase boundaries, especially the boundary of topological SPT phase. The mismatch at the phase boundaries corresponds the state representations incorrectly clustered in Fig. 7a, suggesting our network struggles to learn long-range correlations at phase boundaries.

Generalization to quantum systems of larger size

We now show that our model is capable of extracting features that are transferable across different system sizes. To this purpose, we use a training dataset generated from 10-qubit ground states of the bond-alternating XXZ model (3) and then we use the trained network to generate state representations from the local measurement data of each 50-qubit ground state of (3). Note that, since we use measurements on subsystems of fixed size, the size of the input to our neural network remains constant during both training and testing, independently of the total number of qubits in the system. During training on 10-qubit systems, the network is informed by the index of the first qubit in each qubit triplet, which ranges from 0 to 7. For testing, this index ranges from 0 to 47. This index primarily labels the triplets without carrying specific meaning. Numerical experiments below show that this index does not significantly affect the quality of predictions, likely due to the approximate translational symmetry. Alternatively, one-hot encoding could specify qubit triplets, but this would complicate the neural network and introduce size dependence.

Figure 8a shows that inputting the state representations into the t-SNE algorithm still gives rise to clusters according to the three distinct phases of matter. This observation suggests that the neural network can effectively classify different phases of the bond-alternating XXZ model, irrespective of the system size. In addition to clustering larger quantum states, the representation network also facilitates the prediction of quantum properties in the larger system. To demonstrate this capability, we employ 40 reference ground states of the 50-qubit bond-alternating XXZ model, which are only half size of the training dataset used for 10-qubit system, to train two prediction networks: one for spin correlations and the other for mutual information. Figure 8b shows the coefficients of determination for each prediction, which exhibit values around 0.9 or above. Figure 8b also shows the impact of inaccurate labeling of the ground states on our model. In the reported experiments, we assumed that 10% of the labels in the training dataset corresponding to 40 reference states are randomly incorrect, while the remaining 90% are accurate. Without any mitigation, we observe that the error substantially impacts the accuracy of our predictions. On the other hand, employing a technique of noise mitigation during the training of prediction networks (see Supplementary Note 6) can effectively reduce the impact of the incorrect labels.

Measuring all qubits simultaneously

We now apply our multi-task network to a scenario where all qubits are measured simultaneously with suitable product observables. This scenario is motivated by recent experiments on trapped-ion systems[33,36,37]. In these experiments, the qubits were divided into groups of equal size, and the same product of Pauli observables was measured simultaneously in all groups. Here, we adopt the settings of[33,36], where the groups consist of three neighboring qubits. We consider the ground states of a 50-qubits XXZ model and take $\mathcal{M}$M to be the the set of all 27 measurements that measure the same three-qubit Pauli observable on each triplet. Compared to the set of 3^{50} products of Pauli observables on all qubits, this choice significantly reduces the number of measurement settings the experimenter has to sample from.

As an example, we choose $\mathcal{S} \subset \mathcal{M}$ as the set of three measurements corresponding to the cyclically permuted Pauli strings $\sigma_1^x\sigma_2^y\sigma_3^z\sigma_4^x\sigma_5^y\sigma_6^z\cdots\sigma_{50}^y$, $\sigma_1^y\sigma_2^z\sigma_3^x\sigma_4^y\sigma_5^z\sigma_6^x\cdots\sigma_{50}^z$, and $\sigma_1^z\sigma_2^x\sigma_3^y\sigma_4^z\sigma_5^x\sigma_6^y\cdots\sigma_{50}^x$. For each copy of the quantum state, we randomly sample a measurement from $\mathcal{S}$ to apply to the state and perform a total of 300 measurements. We then use the marginal distributions of the outcomes on every qubit triplet as the input to our representation network to

https://doi.org/10.1038/s41467-024-53101-y

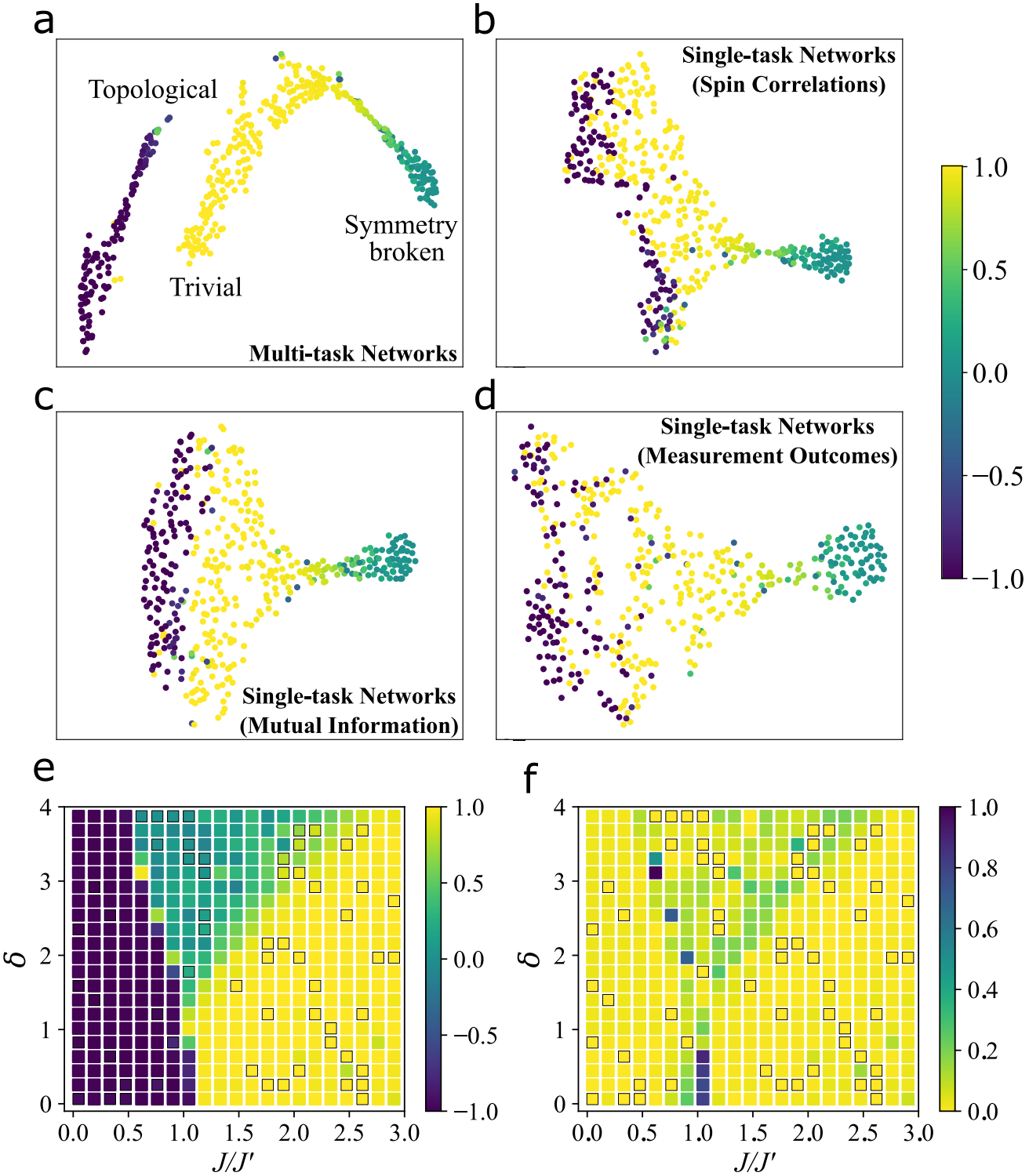

Fig. 7 | 2D projections of the state representations for bond-alternating XXZ model obtained with the t-SNE algorithm and predictions of many-body topological invariants. The color of each data point in Subfigures **a**-**d** indicates the true value of many-body topological invariant $\mathcal{Z}_R$ of the corresponding ground state. Subfigure (**a**) corresponds to the state representations produced for predicting both spin correlations and mutual information. Whereas, Subfigures (**b, c** and **d**) correspond to the state representations produced for predicting spin correlations, mutual information and measurement outcome distributions respectively. Subfigure (**e**) shows the predictions of $\mathcal{Z}_R$ for the ground states corresponding to all pairs of parameters $(J/J', \delta)$ together with the true values of 60 reference states marked by gray squares. The color for each pair of parameters in the phase diagram represents the prediction values. Subfigure (**f**) illustrates the absolute differences between the predictions and the ground truths, where lighter colors indicate smaller differences and darker colors signify larger differences.

produce state representations. Figure 9a shows the 2D projections of our data-driven state representations of 49 ground states of the bond-alternating XXZ model obtained using the t-SNE algorithm, where all three different phases are clearly classified.

It is interesting to compare the performance of our neural network algorithm with the approach of principal component analysis (PCA) with shadow kernel[26]. In the original classical shadow method, measurements are randomly chosen from the set of

https://doi.org/10.1038/s41467-024-53101-y

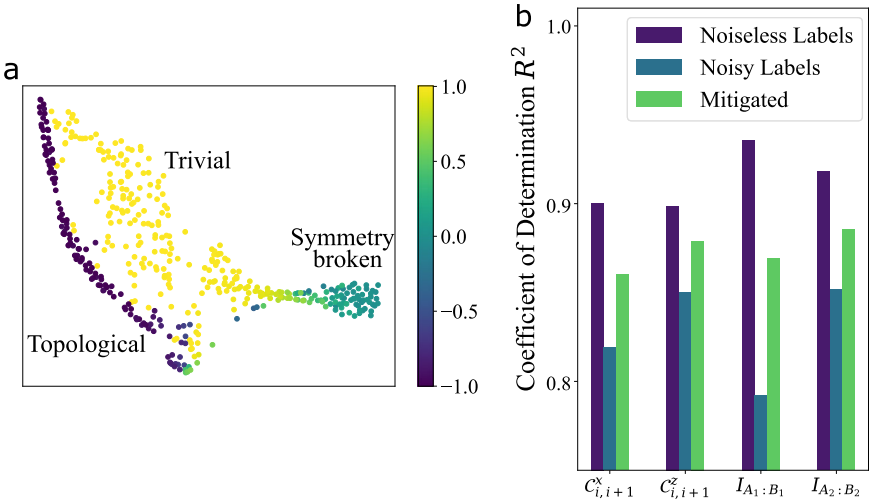

Fig. 8 | Predictions of properties of 50-qubit systems made by a neural network trained over the data of 10-qubit systems. Subfigure (**a**) shows the 2D projections of state representations via t-SNE algorithm. The color of each data point indicates the value of $\mathcal{Z}_R$ on the corresponding state. Subfigure (**b**) shows the coefficient of determination for the predictions of properties using noiseless training labels and noisy training labels, as well as the predictions after error mitigation.

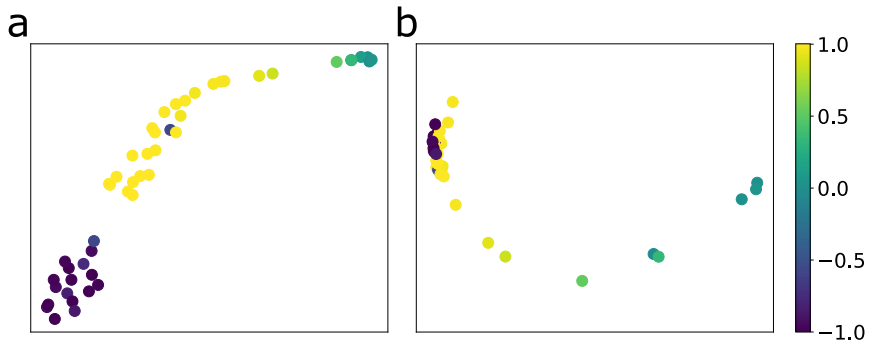

Fig. 9 | Comparison of the state representations from our neural network algorithm and shadow kernel PCA. 2D projections of our data-driven state representations for bond-alternating XXZ model obtained by the t-SNE algorithm (subfigure **a**) and 2D projections of the shadow representations for the same set of states obtained by kernel PCA (subfigure **b**). The color of each data point indicates the value of $\mathcal{Z}_R$ on the corresponding ground state.

all possible Pauli measurements. To make a fair comparison, here we assume that the set of measurements performed in the laboratory is $\mathcal{S}$, the set of measurements used by our method. Figure 9b shows the 2D projections of the shadow representations of the same set of ground states obtained by kernel PCA. The results show that PCA with the shadow kernel can hardly distinguish the topological SPT phase from the trivial SPT phase in this restricted measurement setting. In contrast, our multi-task learning network appears to achieve a good performance in distinguishing the different phases.

Discussion

The use of short-range local measurements is a key distinction between our work and prior approaches approaches using randomized measurements[22–27]. Rather than performing randomized measurements over all spins together, we employ only randomized Pauli measurements detecting short-range correlations. This feature is appealing for practical applications, as measuring only short-range correlations can significantly reduce the number of measurement settings probed in the laboratory. Under restrictions on the set of Pauli measurements sampled in the laboratory, our algorithm outperforms the previous methods using classical shadows. On the other hand, the restriction to short-range local measurements implies that the applicability of our method is limited to many-body quantum states with a constant correlation length, such as ground states within an SPT phase.

A crucial aspect of our neural network model is its ability to generate a latent state representation that integrates different pieces of information, corresponding to multiple physical properties. Remarkably, the state representations appear to capture information about properties beyond those encountered in training. This feature allows for unsupervised classification of phases of matter, applicable not only to in-distribution Hamiltonian ground states but also to out-of-distribution quantum states, like those produced by random circuits. The model also appears to be able to generalize from smaller to larger quantum systems, which makes it an effective tool for exploring intermediate-scale quantum systems.

For new quantum systems, whose true phase diagrams is still unknown, discovering phase diagrams in an unsupervised manner is a major challenge. This challenge can potentially be addressed by combining our neural network with consistency-checking, similar to the approach in ref. 18. The idea is to start with an initial, potentially inaccurate, phase diagram ansatz constructed from limited prior knowledge, for instance, the results of clustering. Then, one can randomly select a set of reference states, labeling them according to the ansatz phases. Based on these labels, a separate neural network is trained to predict phases. Finally, the ansatz can be revised based on the deviation with the network's prediction, and the procedure can be iterated until it

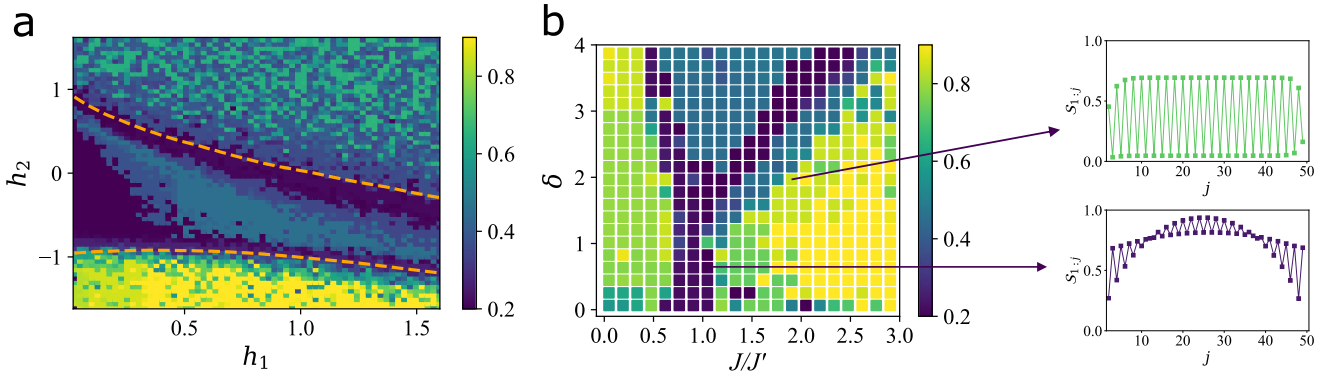

Fig. 10 | A measure of reliability of state representations. Subfigure (**a**) shows the reliability of the representation of each ground state of the cluster-Ising model. Subfigure (**b**) illustrates the reliability of the representation of each ground state of the bond-alternating XXZ model, together with the true subsystem entanglement entropy for two example states: one is near the phase boundary and the other is further away from the phase boundary. In both subfigures, the color in the phase diagram indicates reliability, with lighter colors representing higher reliability and darker colors indicating lower reliability.

converges to a stable ansatz. In Supplementary Note 7, we provide examples of this approach, leaving the development of a full algorithm for autonomous discovery of phase diagram as future work.

Methods

Data generation

Here we illustrate the procedures for generating training and test datasets. For the one-dimensional cluster-Ising model, we obtain measurement statistics and values for various properties in both the training and test datasets through direct calculations, leveraging the ground states solved by exact algorithms. In the case of the one-dimensional bond-alternating XXZ model, we first obtain approximate ground states represented by matrix product states[48,49] using the density-matrix renormalization group (DMRG)[50] algorithm. Subsequently, we compute the measurement statistics and properties by contracting the tensor networks. For the noisy measurement statistics because of finite sampling, we generate them by sampling from the actual probability distribution of measurement outcomes. More details are provided in Supplementary Note 1.

Representation network

The representation network operates on pairs of measurement outcome distributions and the parameterization of their corresponding measurements, denoted as $(\mathbf{d}_i, \mathbf{m}_i)_{i=1}^m$ associated with a state ρ. This network primarily consists of three multilayer perceptrons (MLPs)[51]. The first MLP comprises a four-layer architecture that transforms the measurement outcome distribution into $\mathbf{h}_i^d$, whereas the second two-layer MLP maps the corresponding $\mathbf{m}_i$ to $\mathbf{h}_i^m$:

$$\mathbf{h}_i^d = \mathrm{MLP}_1(\mathbf{d}_i),$$
$$\mathbf{h}_i^m = \mathrm{MLP}_2(\mathbf{m}_i).$$

Next, we merge $\mathbf{h}_i^d$ and $\mathbf{h}_i^m$, feeding them into another three-layer MLP to obtain a partial representation denoted as $\mathbf{r}_i$ for the state:

$$\mathbf{r}_\rho^{(i)} = \mathrm{MLP}_3\left(\left[\mathbf{h}_i^d, \mathbf{h}_i^m\right]\right). \tag{5}$$

Following this, we aggregate all the $\mathbf{r}_i$ representations through an average pooling layer to produce the complete state representation, denoted as $\mathbf{r}_\rho$:

$$\mathbf{r}_\rho = \frac{1}{s}\sum_{i=1}^{s} \mathbf{r}_i. \tag{6}$$

Alternatively, we can leverage a recurrent neural network equipped with gated recurrent units (GRUs)[52] to derive the comprehensive state representation from the set $\{\mathbf{r}_i\}_{i=1}^m$:

$$\mathbf{z}_i = \mathrm{sigmoid}\left(W_z \mathbf{r}_\rho^{(i)} + U_z \mathbf{r}_\rho^{(i-1)} + \mathbf{b}_\mathbf{z}\right),$$
$$\hat{\mathbf{h}}_i = \tanh\left(W_h \mathbf{r}_\rho^{(i)} + U_h(\mathbf{z}_i \odot \mathbf{h}_{i-1}) + \mathbf{b}_\mathbf{h}\right),$$
$$\mathbf{h}_i = (1 - \mathbf{z}_i) \odot \mathbf{h}_{i-1} + \mathbf{z}_i \odot \hat{\mathbf{h}}_i,$$
$$\mathbf{r}_\rho = \mathbf{h}_m,$$

where W, U, $\mathbf{b}$ are trainable matrices and vectors. The architecture of the recurrent neural network offers a more flexible approach to generate the complete state representation; however, in our experiments, we did not observe significant advantages compared to the average pooling layer.

Reliability of Representations

The neural network can assess the reliability of each state representation by conducting contrastive analysis within the representation space. Figure 10 shows a measure of the reliability of each state representation, which falls in the region [0, 1], for both the cluster-Ising model and the bond-alternating XXZ model. As this measure increases from 0 to 1, the reliability of the corresponding prediction strengthens, with values closer to 0 indicating low reliability and values closer to 1 indicating high reliability. Figure 10a indicates that the neural network exhibits lower confidence for the ground states in SPT phase than those in the other two phases, with the lowest confidence occurring near the phase boundaries. Figure 10b shows that the reliability of predictions for the ground states of the XXZ model in two SPT phases are higher than those in the symmetry broken phase, which is due to the imbalance of training data, and that the predictions for quantum states near the phase boundaries have the lowest reliability. Here, the reliability is associated with the distance between the state representation and its cluster center in the representation space. We adopt this definition based on the intuition that for a quantum state that the model should exhibit higher confidence for quantum states that cluster more easily.

Distance-based methods[53,54] have proven effective in the task of Out-of-Distribution detection in classical machine learning. This task focuses on identifying instances that significantly deviate from the data distribution observed during training, thereby potentially compromising the reliability of the trained neural network. Motivated by this line of research, we present a contrastive methodology for assessing the reliability of representations produced by the proposed neural model. Denote the set of representations corresponding quantum states as $\{\mathbf{r}_{\rho_1}, \mathbf{r}_{\rho_2}, \cdots, \mathbf{r}_{\rho_n}\}$. We leverage reachability distances, $\{d_{\rho_j}\}_{j=1}^n$, derived from the OPTICS (Ordering Points To Identify the

Clustering Structure) clustering algorithm[55] to evaluate the reliability of representations, denoted as $\{rv_{\rho_j}\}_{j=1}^n$:

$$\{d_{\rho_j}\}_{j=1}^n = \mathrm{OPTICS}\left(\{\phi(\mathbf{r}_{\rho_j})\}_{j=1}^n\right),$$
$$rv_{\rho_j} = \frac{\exp(-d_{\rho_k})}{\max_{k=1}^n \exp(-d_{\rho_k})},$$

where ϕ is a feature encoder. In the OPTICS clustering algorithm, a smaller reachability distance indicates that the associated point lies closer to the center of its corresponding cluster, thereby facilitating its clustering process. Intuitively, a higher density within a specific region of the representation space indicates that the trained neural model has had more opportunities to gather information from that area, thus enhancing its reliability. Our proposed method is supported by similar concepts introduced in ref. 54. More details are provided in Supplementary Note 3.

Prediction Network

For each type of property associated with the state, we employ a dedicated prediction network responsible for making predictions. Each prediction network is composed of three MLPs. The first MLP takes the state representation $\mathbf{r}_\rho$ as input and transforms it into a feature vector $\mathbf{h}^{\mathbf{r}}$ while the second takes the query task index q as input and transforms it into a feature vector $\mathbf{h}^q$. The second MLP operates on the combined feature vectors $[\mathbf{h}^{\mathbf{r}}, \mathbf{h}^q]$ to produce the prediction $f_q(\rho)$ for the property under consideration:

$$\mathbf{h}^{\mathbf{r}} = \mathrm{MLP}_4(\mathbf{r}_\rho),$$
$$\mathbf{h}^q = \mathrm{MLP}_5(q),$$
$$f_q(\rho) = \mathrm{MLP}_6([\mathbf{h}^{\mathbf{r}}, \mathbf{h}^q]).$$

Network training

We employ the stochastic gradient descent[56] optimization algorithm and the Adam optimizer[57] to train our neural network. In our training procedure, for each state within the training dataset, we jointly train both the representation network and the prediction networks associated with one or two types of properties available for that specific state. The training loss is the cumulative sum of losses across different states and properties. This training is achieved by minimizing the difference between the predicted values generated by the network and the ground-truth values, thus refining the model's ability to capture and reproduce the desired property characteristics. The detailed pseudocode for the training process can be found in Supplementary Note 2.

Network Test & Transfer Learning

After the training is concluded, the multi-task networks are fixed. To evaluate the performance of the trained model, we perform a series of tests on a separate dataset that includes states not seen during training. This evaluation helps in assessing the model's ability to generalize to new data. To achieve transfer learning for new tasks using state representations produced by the representation network, we first fix the representation network and obtain the state representations. We then introduce a new prediction network that takes these state representations as input, allowing us to leverage the pre-trained representations to predict new properties. During the training of this new task, we use the Adam optimizer[57] and stochastic gradient descent[56] to minimize the prediction error. Once the training is complete, we fix this new prediction network and test its performance on previously unseen states to evaluate its generalization capability.

Hardware

We employ the PyTorch framework[58] to construct the multi-task neural networks in all our experiments and train them with two NVIDIA GeForce GTX 1080 Ti GPUs.

Data availability

Data sets generated during the current study are available in https://github.com/yzhuqici/learn_quantum_properties_from_local_correlation.

Code availability

The codes that support the findings of this study are available in https://github.com/yzhuqici/learn_quantum_properties_from_local_correlation.

References

1. Torlai, G. et al. Neural-network quantum state tomography. *Nat. Phys.* **14**, 447–450 (2018).
2. Carrasquilla, J., Torlai, G., Melko, R. G. & Aolita, L. Reconstructing quantum states with generative models. *Nat. Mach. Intell.* **1**, 155–161 (2019).
3. Zhu, Y. et al. Flexible learning of quantum states with generative query neural networks. *Nat. Commun.* **13**, 6222 (2022).
4. Schmale, T., Reh, M. & Gärttner, M. Efficient quantum state tomography with convolutional neural networks. *NPJ Quantum Inf.* **8**, 115 (2022).
5. Carleo, G. & Troyer, M. Solving the quantum many-body problem with artificial neural networks. *Science* **355**, 602–606 (2017).
6. Zhang, X. et al. Direct fidelity estimation of quantum states using machine learning. *Phys. Rev. Lett.* **127**, 130503 (2021).
7. Xiao, T., Huang, J., Li, H., Fan, J. & Zeng, G. Intelligent certification for quantum simulators via machine learning. *NPJ Quantum Inf.* **8**, 138 (2022).
8. Du, Y. et al. Shadownet for data-centric quantum system learning. *arXiv preprint arXiv:2308.11290* (2023).
9. Wu, Y.-D., Zhu, Y., Bai, G., Wang, Y. & Chiribella, G. Quantum similarity testing with convolutional neural networks. *Phys. Rev. Lett.* **130**, 210601 (2023).
10. Qian, Y., Du, Y., He, Z., Hsieh, M.-H. & Tao, D. Multimodal deep representation learning for quantum cross-platform verification. *Phys. Rev. Lett.* **133**, 130601 (2024).
11. Gao, J. et al. Experimental machine learning of quantum states. *Phys. Rev. Lett.* **120**, 240501 (2018).
12. Gray, J., Banchi, L., Bayat, A. & Bose, S. Machine-learning-assisted many-body entanglement measurement. *Phys. Rev. Lett.* **121**, 150503 (2018).
13. Koutnỳ, D. et al. Deep learning of quantum entanglement from incomplete measurements. *Sci. Adv.* **9**, eadd7131 (2023).
14. Torlai, G. et al. Integrating neural networks with a quantum simulator for state reconstruction. *Phys. Rev. Lett.* **123**, 230504 (2019).
15. Huang, Y. et al. Measuring quantum entanglement from local information by machine learning. *arXiv preprint arXiv:2209.08501* (2022).
16. Smith, A. W. R., Gray, J. & Kim, M. S. Efficient quantum state sample tomography with basis-dependent neural networks. *PRX Quantum* **2**, 020348 (2021).
17. Carrasquilla, J. & Melko, R. G. Machine learning phases of matter. *Nat. Phys.* **13**, 431–434 (2017).
18. Van Nieuwenburg, E. P., Liu, Y.-H. & Huber, S. D. Learning phase transitions by confusion. *Nat. Phys.* **13**, 435–439 (2017).
19. Huembeli, P., Dauphin, A. & Wittek, P. Identifying quantum phase transitions with adversarial neural networks. *Phys. Rev. B* **97**, 134109 (2018).
20. Rem, B. S. et al. Identifying quantum phase transitions using artificial neural networks on experimental data. *Nat. Phys.* **15**, 917–920 (2019).

21. Kottmann, K., Huembeli, P., Lewenstein, M. & Acín, A. Unsupervised phase discovery with deep anomaly detection. *Phys. Rev. Lett.* **125**, 170603 (2020).
22. Huang, H.-Y., Kueng, R. & Preskill, J. Predicting many properties of a quantum system from very few measurements. *Nat. Phys.* **16**, 1050–1057 (2020).
23. Elben, A. et al. Cross-platform verification of intermediate scale quantum devices. *Phys. Rev. Lett.* **124**, 010504 (2020).
24. Elben, A. et al. Many-body topological invariants from randomized measurements in synthetic quantum matter. *Sci. Adv.* **6**, eaaz3666 (2020).
25. Huang, H.-Y. Learning quantum states from their classical shadows. *Nat. Rev. Phys.* **4**, 81–81 (2022).
26. Huang, H.-Y., Kueng, R., Torlai, G., Albert, V. V. & Preskill, J. Provably efficient machine learning for quantum many-body problems. *Science* **377**, eabk3333 (2022).
27. Elben, A. et al. The randomized measurement toolbox. *Nat. Rev. Phys.* **5**, 9–24 (2023).
28. Zhao, H. et al. Learning quantum states and unitaries of bounded gate complexity. *arXiv preprint arXiv:2310.19882* (2023).
29. Hu, H.-Y., Choi, S. & You, Y.-Z. Classical shadow tomography with locally scrambled quantum dynamics. *Phys. Rev. Res.* **5**, 023027 (2023).
30. Hu, H.-Y. et al. Demonstration of robust and efficient quantum property learning with shallow shadows. *arXiv preprint arXiv:2402.17911* (2024).
31. Cramer, M. et al. Efficient quantum state tomography. *Nat. Commun.* **1**, 149 (2010).
32. Baumgratz, T., Nüßeler, A., Cramer, M. & Plenio, M. B. A scalable maximum likelihood method for quantum state tomography. *N. J. Phys.* **15**, 125004 (2013).
33. Lanyon, B. et al. Efficient tomography of a quantum many-body system. *Nat. Phys.* **13**, 1158–1162 (2017).
34. Kurmapu, M. K. et al. Reconstructing complex states of a 20-qubit quantum simulator. *PRX Quantum* **4**, 040345 (2023).
35. Guo, Y. & Yang, S. Quantum state tomography with locally purified density operators and local measurements. *Commun. Phys.* **7**, 322 (2024).
36. Friis, N. et al. Observation of entangled states of a fully controlled 20-qubit system. *Phys. Rev. X* **8**, 021012 (2018).
37. Joshi, M. K. et al. Exploring large-scale entanglement in quantum simulation. *Nature* **624**, 539–544 (2023).
38. Zhang, Y. & Yang, Q. A survey on multi-task learning. *IEEE Trans. Knowl. Data Eng.* **34**, 5586–5609 (2021).
39. Klyachko, A. A. et al. Quantum marginal problem and n-representability. *J. Physi.: Conf. Series*, **36**, 72 (IOP Publishing, 2006).
40. Christandl, M. & Mitchison, G. The spectra of quantum states and the kronecker coefficients of the symmetric group. *Commun. Math. Phys.* **261**, 789–797 (2006).
41. Schilling, C. et al. *The Quantum Marginal Problem*. In *Mathematical Results in Quantum Mechanics: Proceedings of the QMath12 Conference*, 165–176 (World Scientific, 2015).
42. Pollmann, F. & Turner, A. M. Detection of symmetry-protected topological phases in one dimension. *Phys. Rev. B* **86**, 125441 (2012).
43. Smacchia, P. et al. Statistical mechanics of the cluster Ising model. *Phys. Rev. A* **84**, 022304 (2011).
44. Cong, I., Choi, S. & Lukin, M. D. Quantum convolutional neural networks. *Nat. Phys.* **15**, 1273–1278 (2019).
45. Herrmann, J. et al. Realizing quantum convolutional neural networks on a superconducting quantum processor to recognize quantum phases. *Nat. Commun.* **13**, 4144 (2022).
46. Cohen, P. R. & Howe, A. E. How evaluation guides ai research: the message still counts more than the medium. *AI Mag.* **9**, 35–35 (1988).
47. Liu, Y.-J., Smith, A., Knap, M. & Pollmann, F. Model-independent learning of quantum phases of matter with quantum convolutional neural networks. *Phys. Rev. Lett.* **130**, 220603 (2023).
48. Fannes, M., Nachtergaele, B. & Werner, R. F. Finitely correlated states on quantum spin chains. *Commun. Math. Phys.* **144**, 443–490 (1992).
49. Perez-García, D., Verstraete, F., Wolf, M. M. & Cirac, J. I. Matrix product state representations. *Quantum Inf. Comput.* **7**, 401–430 (2007).
50. Schollwöck, U. The density-matrix renormalization group. *Rev. Mod. Phys.* **77**, 259 (2005).
51. Gardner, M. W. & Dorling, S. Artificial neural networks (the multilayer perceptron)—a review of applications in the atmospheric sciences. *Atmos. Environ.* **32**, 2627–2636 (1998).
52. Chung, J., Gulcehre, C., Cho, K. & Bengio, Y. Empirical evaluation of gated recurrent neural networks on sequence modeling. In *NIPS 2014 Workshop on Deep Learning, December 2014* (2014).
53. Lee, K., Lee, K., Lee, H. & Shin, J. A simple unified framework for detecting out-of-distribution samples and adversarial attacks. *Advances in neural information processing systems* **31,** (2018).
54. Sun, Y., Ming, Y., Zhu, X. & Li, Y. Out-of-distribution detection with deep nearest neighbors. In *International Conference on Machine Learning*, 20827–20840 (PMLR, 2022).
55. Ankerst, M., Breunig, M. M., Kriegel, H.-P. & Sander, J. Optics: Ordering points to identify the clustering structure. *ACM Sigmod Rec.* **28**, 49–60 (1999).
56. Bottou, L. et al. Stochastic gradient descent tricks. In *Neural Networks: Tricks of the Trade: Second Edition*, 421–436 (Springer, 2012).
57. Kingma, D. P. & Ba, J. Adam: A method for stochastic optimization. *arXiv preprint arXiv:1412.6980* (2014).
58. Paszke, A. et al. Pytorch: An imperative style, high-performance deep learning library. *Advances in neural information processing systems***32** (2019).
59. Williamson, D. F., Parker, R. A. & Kendrick, J. S. The box plot: a simple visual method to interpret data. *Ann. Intern. Med.* **110**, 916–921 (1989).

Acknowledgements

We thank Ge Bai, Dong-Sheng Wang, Shuo Yang, Yuchen Guo and Jiehang Zhang for the helpful discussions on many-body quantum systems. This work was supported by funding from the Hong Kong Research Grant Council through grants no. 17300918 and no. 17307520 (GC), through the Senior Research Fellowship Scheme SRFS2021-7S02 (GC), the Chinese Ministry of Science and Education through grant 2023ZD0300600 (GC), and the John Templeton Foundation through grant 62312 (GC), The Quantum Information Structure of Spacetime (qiss.fr). YDW acknowledges funding from the National Natural Science Foundation of China through grants no. 12405022. YXW acknowledges funding from the National Natural Science Foundation of China through grants no. 61872318. Research at the Perimeter Institute is supported by the Government of Canada through the Department of Innovation, Science and Economic Development Canada and by the Province of Ontario through the Ministry of Research, Innovation and Science. The opinions expressed in this publication are those of the authors and do not necessarily reflect the views of the John Templeton Foundation.

Author contributions

Y.-D.W. and Y.Z. developed the key idea for this paper. Y.Z. conducted the numerical experiments while G.C. and Y.W. contributed to their design. All coauthors contributed to the writing of the manuscript.

Competing interests

The authors declare no competing interests.

Additional information

Supplementary information The online version contains supplementary material available at https://doi.org/10.1038/s41467-024-53101-y.

Correspondence and requests for materials should be addressed to Yan Zhu or Giulio Chiribella.

Peer review information *Nature Communications* thanks Alistair Smith, and the other, anonymous, reviewers for their contribution to the peer review of this work. A peer review file is available.

Reprints and permissions information is available at http://www.nature.com/reprints

Publisher's note Springer Nature remains neutral with regard to jurisdictional claims in published maps and institutional affiliations.

Open Access This article is licensed under a Creative Commons Attribution-NonCommercial-NoDerivatives 4.0 International License, which permits any non-commercial use, sharing, distribution and reproduction in any medium or format, as long as you give appropriate credit to the original author(s) and the source, provide a link to the Creative Commons licence, and indicate if you modified the licensed material. You do not have permission under this licence to share adapted material derived from this article or parts of it. The images or other third party material in this article are included in the article's Creative Commons licence, unless indicated otherwise in a credit line to the material. If material is not included in the article's Creative Commons licence and your intended use is not permitted by statutory regulation or exceeds the permitted use, you will need to obtain permission directly from the copyright holder. To view a copy of this licence, visit http://creativecommons.org/licenses/by-nc-nd/4.0/.

© The Author(s) 2024